J Mater Sci (2010) 45:4718–4724
DOI 10.1007/s10853-010-4588-z

ULTRAFINE GRAINED MATERIALS

Unusual super-ductility at room temperature in an ultrafine-grained aluminum alloy

Ruslan Z. Valiev · Maxim Yu. Murashkin · Askar Kilmametov · Boris Straumal · Nguyen Q. Chinh · Terence G. Langdon

Received: 9 April 2010 / Accepted: 30 April 2010 / Published online: 15 May 2010

Abstract Processing by severe plastic deformation (SPD) typically increases the strength of metals and alloys drastically by decreasing their grain size into the submicrometer or nanometer range but the ductility of such materials remains typically low. This report describes the first demonstration that it is possible to increase the room temperature ductility of aluminum-based alloys processed by SPD and to attain elongations to failure of >150% while retaining the enhanced strength. This unique combination of properties is due to the occurrence of grain boundary sliding at room temperature. The sliding was obviously achieved by introducing a grain boundary wetting of the aluminum/aluminum grain boundaries.

R. Z. Valiev (✉) · M. Yu. Murashkin · A. Kilmametov
Institute of Physics of Advanced Materials, Ufa State Aviation Technical University, 12 K. Marx str., Ufa, Russia 450000
e-mail: rzvaliev@mail.rb.ru

B. Straumal
Institute of Solid State Physics, Russian Academy of Sciences, Chernogolovka, Moscow district 142432, Russia

B. Straumal
Max-Planck-Institut für Metallforschung, Heisenbergstrasse 3, 70569 Stuttgart, Germany

N. Q. Chinh
Department of Materials Physics, Eötvös Loránd University, Pázmány Péter s. 1/A, Budapest 1117, Hungary

T. G. Langdon
Departments of Aerospace & Mechanical Engineering and Materials Science, University of Southern California, Los Angeles, CA 90089-1453, USA

T. G. Langdon
Materials Research Group, School of Engineering Sciences, University of Southampton, Southampton SO17 1BJ, UK

Introduction

It is now well established that processing by severe plastic deformation (SPD) promotes grain refinement and formation of the ultrafine-grained (UFG) materials with mean grain sizes in the submicrometer or nanometer range [1, 2]. Several recent investigations demonstrate also that the UFG metals and alloys generally exhibit increased strength but low ductility at room temperature [3, 4]. The low ductility at ambient temperature restricts the use of these materials for structural applications. That is why the enhancement of the ductility of UFG materials is quite a topical problem and several different strategies have been developed recently to improve the materials' poor ductility, including the introduction of a grain size distribution [5], the preexisting nanoscale twins [6, 7], dispersions of nanoparticles and nanoprecipitates [8, 9], transformation- and twinning-induced plasticities [10, 11] and some others. These approaches are based on the increase of strain hardening through dislocation storage capacity during deformation. At the same time, the enhancement of the ductility of UFG materials may be achieved also at the expense of enhanced strain-rate hardening, when diffusion-controlled grain boundary (GB) sliding becomes active [12]. For example, it is applied at elevated temperatures where UFG materials exhibit superplastic behavior at higher strain rates [13, 14]. In this work, we for the first time demonstrate the possibilities of enhancement of strain-rate hardening and ductility in the UFG Al alloy at room temperature by stimulating GB sliding due to maintaining a high GB diffusion flux and the appearance of a GB wetting phase.

Experimental

The test material was an aluminum-based alloy containing 30 wt% Zn prepared from high purity components (99.9995% Al and 99.999% Zn) by vacuum induction melting. As-cast disks of the alloy were prepared by grinding and chemical etching and they were then homogenized at 500 °C for 5 h and processed by high-pressure torsion (HPT) at room temperature under an imposed pressure of 6.0 GPa using a special HPT die [15, 16], which enables to process samples of diameters of 20 mm and thicknesses of ~0.8 mm. The straining was continued through a total of five turns at a rotation speed of 1 rpm. After HPT of the homogenized samples, the central part of each disk, having a diameter of ~5 mm, was excluded from any further investigation. Samples for structural investigations were cut from the HPT disks at a distance of 5 mm from the sample center where this distance corresponds to a shear strain of ~6. Transmission electron microscopy (TEM) was used with a JEOL-2000EX microscope at an accelerating voltage of 120 kV. X-ray phase analysis was performed using a Pan Analytical X'Pert (Philips) diffractometer in Bragg-Brentano geometry with Cu Kα radiation and a position-sensitive detector (Philips X'Cellerator). The Profit (Philips) software was used for X-ray peak profiles fitting and estimation of the lattice parameter, microstrain value and coherently scattering region size. The average dislocation density was derived using the well-known X-ray diffraction procedure [17]. Mechanical tensile testing was conducted at room temperature at strain rates from 10^{-4} to 10^{-2} s^{-1}. Samples for mechanical tests were spark-cut excluding the central part (~5 mm in diameter) of the HPT-processed disks in order to avoid the microstructural inhomogeneities. The testing conditions of temperature, strain rate, and load were controlled by computer software to within an error of 2–3%. The yield strength, $\sigma_{0.2}$, ultimate strength, σ_B, and ductility or relative elongation to failure, δ, were determined from the results of tests conducted on at least three samples having gauge dimensions of 4.0 × 1.0 × 0.4 mm^3.

Following either annealing or annealing together with processing by HPT, specimens were prepared for examination using a microindenter. Each sample was electropolished at room temperature using a solution of 33% HNO_3 and 67% CH_3OH. Micro-indentations were made at room temperature with a Vickers diamond microindenter using a depth-sensing ultra-microhardness testing machine (Shimadzu DUH 202) operating under a force, F, that increased linearly with time, t, using an imposed loading rate, ν_l, between 0.7 and 70 mN s^{-1}. It may be estimated from an earlier analysis [18] that the loading rate in this region corresponds to an equivalent strain rate between 5×10^{-4} and 5×10^{-2} s^{-1} around the edge of the indenter at the end of the indentation process.

After indentation, the changes in the surface topographies were examined around the indentations using an atomic force microscope (Solver P47H) operating in the semi-contact (frequency-modulation) mode with conductive silicon cantilevers having a resonant eigenfrequency of 120–190 kHz. In order to optimize the subsequent observations using AFM, it was necessary to consider both the average grain size of the ultrafine-grained sample (~0.4 μm) and the area available in the microscope for high-resolution images (~20 × 20 μm^2). It is apparent that optimum results will be achieved if the indentation pattern and the surrounding area are both contained within the area of observation for the AFM. Repetitive indentations with different loads revealed an optimum condition for the HPT sample where the maximum load used in the indenter was 35 mN to give a depth of about 1 μm and a Vickers pattern extending over an area of ~6 × 6 μm^2. For the annealed sample, where the material was significantly harder because of the presence of a solid solution, the optimum load was 50 mN to give an indentation having a reasonably similar size as in the HPT sample.

Results and discussions

After homogenization annealing, the solid solution microstructure had equiaxed grains with a mean size of ~65 μm. After SPD processing by HPT, the Al-based solid solution dissociated and X-ray diffraction (XRD) spectra contained only the peaks of pure Al and Zn. A similar dissociation of a supersaturated solid solution after HPT was previously reported in as-cast Al–Zn alloys [19]. The microstructure after HPT contained equiaxed ultrafine Al grains having a size of ~380 nm as shown in Fig. 1a. Smaller Zn grains having sizes between ~50 and ~150 nm were located at the triple junctions of the aluminum grains as shown in Fig. 1b. Furthermore, minor amounts of Zn, with sizes of ~5–15 nm, were also present within the aluminum grains. The XRD peaks of Al revealed low microstrain contributions in the peak broadening with microstrain levels of ~0.010 ± 0.002%. Using XRD, the average dislocation density was estimated as ~10^{12} m^{-2} where this value correlates well with conventional data from transmission electron microscopy (TEM) showing the aluminum grains are almost free of lattice dislocations. The evolution of microstructure correlates with the variation in the microhardness. Thus, the microhardness was ~1670 MPa in the homogenized and quenched state and decreased to ~490 MPa after HPT. These measurements show that processing by HPT gives a significant softening of the samples due to decomposition in HPT of the Zn-rich

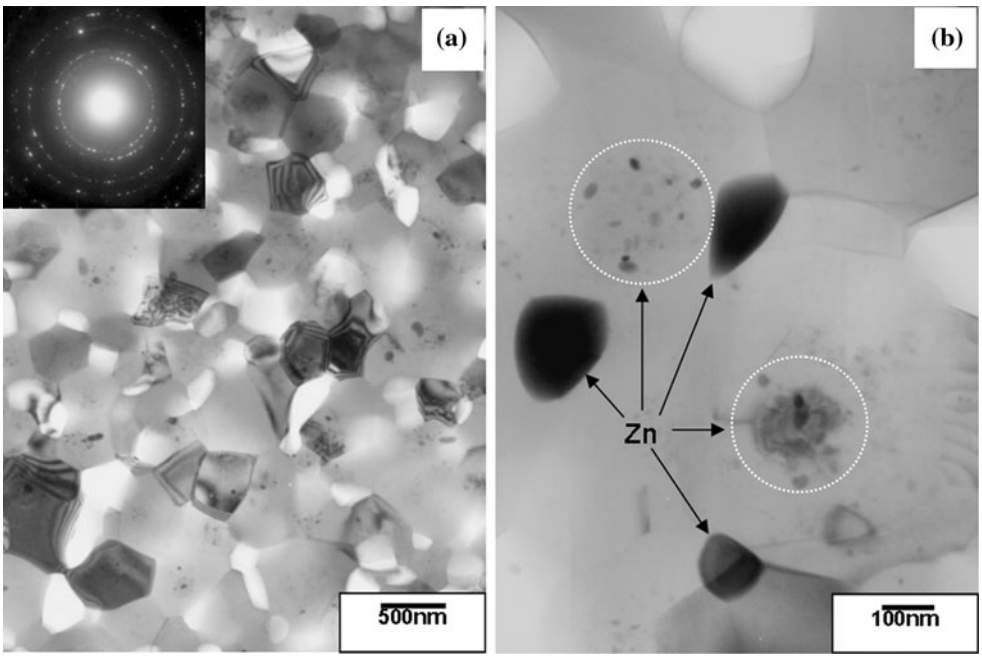

Fig. 1 **a** Microstructure of the Al–30 wt% Zn alloy formed in the billet processed by HPT and **b** Zn phase precipitates at triple junctions and within the Al grains

Al-based solid solution. A similar softening in HPT was reported earlier for as-cast Al–Zn alloys [20].

Experimental results obtained by tensile testing show both the flow stress, σ, and the maximum elongation to failure, δ, depend strongly on the imposed strain rate, $\dot{\varepsilon}$, as demonstrated in Fig. 2a. After HPT, the ultrafine-grained Al alloy exhibits unusually high ductility at room temperature with a maximum elongation of $\sim$160% when testing at $\dot{\varepsilon} \approx 10^{-4}$ s^{-1}. The dependence of the maximum flow stress, σ_{max}, on strain rate is shown in Fig. 2b where the values of the strain rate sensitivity, m, are also given. It can be seen that the strain rate sensitivity for strain rates between $\sim 10^{-3}$ and $\sim 10^{-4}$ s^{-1} is high and of the order of $m \approx 0.24$–0.29. Such high values of m are close to those anticipated for a process such as the viscous glide of dislocations where $m \approx 0.33$ but usually this is found only in conditions of high temperature creep at temperatures above $\sim 0.5\ T_m$, where T_m is the absolute melting temperature.

Applying depth-sensing indentations at different loading rates after HPT, the enhanced strain rate sensitivity, $m = 0.22$, for the Al–30 wt% Zn sample was also measured, while for similar samples not processed by HPT the strain rate sensitivity was very low and of the order of $\sim$0.04. It should be noted that in general the strain rate sensitivity of ultrafine-grained Al [21] and other fcc metals such as Cu and Ni [22] is very low and lies between 0.01 and 0.03. The δ and m values obtained in this investigation after HPT reveal the development of a super-ductility at room temperature. Such behavior was not previously

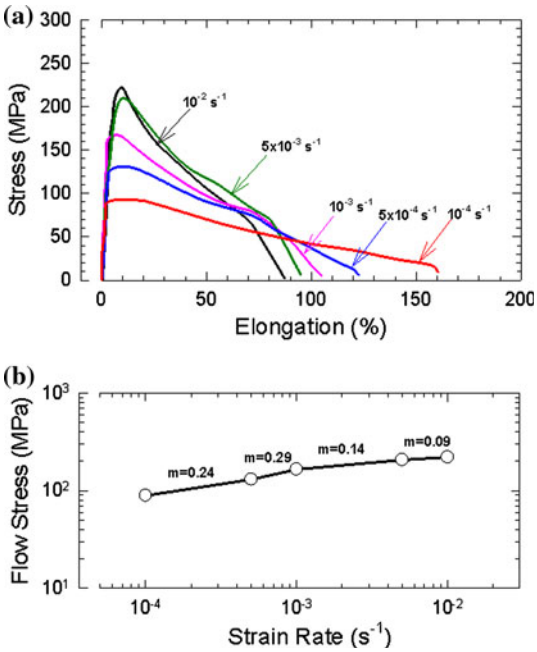

Fig. 2 **a** Effect of strain rate on the true stress–strain curves and **b** the variation of flow stress with strain rate and the values of the strain rate sensitivity, m, for the Al–30 wt% Zn alloy processed by HPT

reported in any Al-based alloys at this low temperature. It should also be emphasized that the microstructure of the HPT-processed Al–30 wt% Zn samples remains stable during deformation. No grain growth was observed during the indentation taking place for different dwell times from

15 up to 1500 s. This microstructural stability is an important advantage of the investigated ultrafine-grained alloy against some nanocrystalline metals, which have instable microstructure leading to fast grain growth and also softening during relatively short dwell times of the indenter [23, 24].

Figure 3 shows typical atomic force microscopy (AFM) images of the surfaces of samples after indentation with a Vickers microindenter for (a) the annealed or recovered condition and (b) after processing by HPT: the scales on the right denote the vertical levels on the images. Qualitatively, both indentations are of a similar size with lateral edges of ~6 μm but the morphologies of the surrounding surfaces are different. For the recovered condition in Fig. 3a, where the size of the Vickers pattern is much smaller than the average grain size of ~70 μm, the surface surrounding the indentation is relatively smooth, whereas after HPT in Fig. 3b the surrounding area shows small grains having sizes of ~400 nm. It will be shown through detailed measurements that this apparent rumpling corresponds to the displacements of individual ultrafine grains within the crystalline matrix.

Quantitative measurements were undertaken on both of these samples by recording the surface height profiles from points located on the edges of the indentations, following the two separate sampling paths labeled "Recovered" in Fig. 3a and "HPT-deformed" in Fig. 3b. The height profiles were determined along each path using implemented software and the results recorded in the form of plots of the vertical profile against the position from the edge of the Vickers pattern. Representative measured profiles, designated h_m, are shown in Fig. 4 and they were fitted using a 9-order polynomial to give the global profile [25, 26], designated h_g, which are shown by the smooth curves in Fig. 4. Considering the global characteristics of the deformation processes, these scans demonstrate that, for both conditions, the values of h_g decrease with increasing distance from the indentation because of the enhanced deformation occurring at the peripheries of the indentations for all ductile metals [27].

In order to study the nature of the deformation processes, it is necessary to consider the local vertical deviations from the global behavior which are defined quantitatively at any position by the value of the term $(h_m - h_g)$. These values are plotted in Fig. 5a, b for the same sampling paths and, for easy comparison, all data are plotted using the same scale. For the recovered sample in Fig. 5a, the perturbations in the vertical scale, with maximum heights of ~5–7 nm, correspond to the general roughness of the polished surface. By contrast, for the HPT-deformed sample in Fig. 5b the perturbations display larger oscillations and there are local maxima or minima occurring at relatively regular intervals of the order

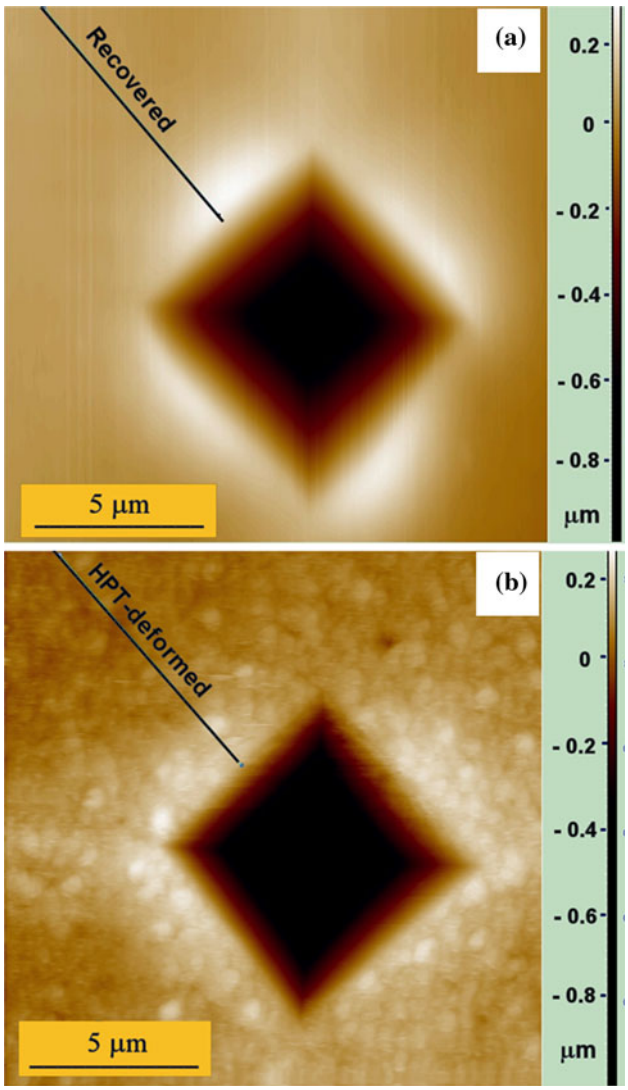

Fig. 3 Indentations produced on the polished surfaces of Al–30 wt% Zn in **a** the recovered condition and **b** after HPT processing: the scales on the right denote the vertical levels and the surface height profiles were recorded along the labeled paths

of ~0.5 μm which correlate with the measured grain size of ~0.4–0.5 μm. The larger displacements recorded in Fig. 5b have heights up to a maximum of ~40 nm and, since they occur at discrete intervals of ~0.5 μm, they must correspond to the relative movements of adjacent grains in the vicinity of the indentation. These repetitive oscillations provide direct evidence for the occurrence of extensive grain boundary sliding during dynamic indentation of the ultrafine-grained Al–Zn sample.

Typical profiles across the Vickers microhardness patterns are shown in Fig. 6 for samples in both conditions. There is a significant difference in the shapes of the piled-up material for these two samples. While the material formed in the case of the recovered sample is only short-term in nature and is sharply defined only in the immediate

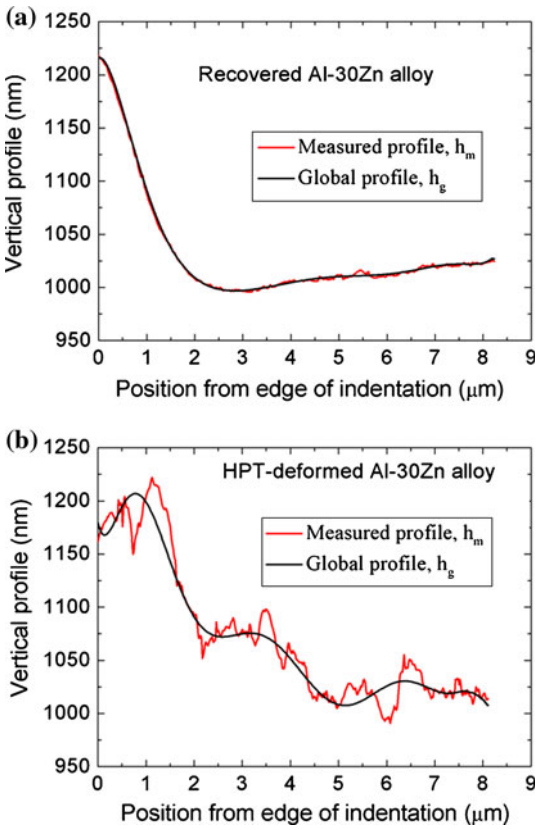

Fig. 4 Plots of the vertical profiles against the position from the edge of the Vickers pattern for **a** the recovered condition and **b** the HPT-deformed state

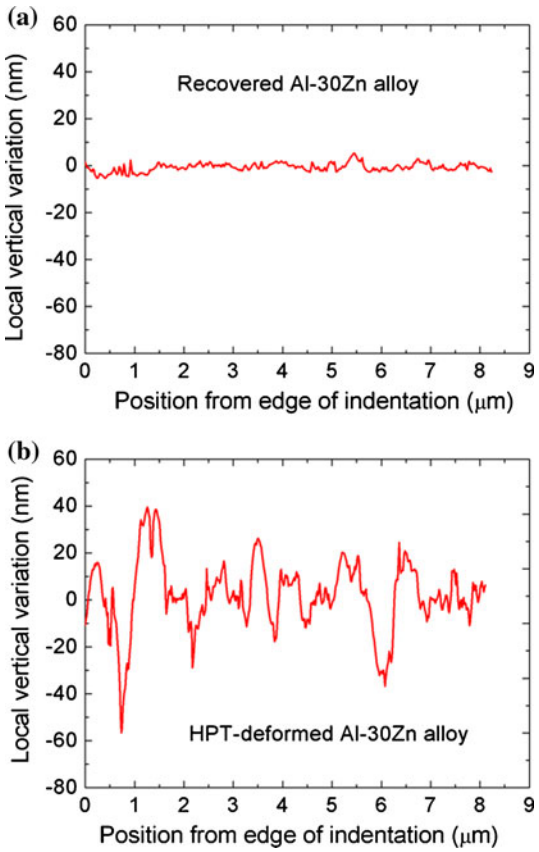

Fig. 5 Plots of the local vertical variations against the position from the edge of the Vickers pattern for **a** the recovered condition and **b** the HPT-deformed state

vicinity of the Vickers pattern, the material associated with the HPT-deformed sample is relatively long-term and spreads out over several micrometers from the indentation. This behavior is a direct consequence of the relatively high strain rate sensitivity in this sample.

Due to the vertical movement of the ultrafine grains in the HPT sample, the areas of piled-up material observed around the Vickers indentations in this sample, labeled $A_{\mathrm{HPT,left}}$ and $A_{\mathrm{HPT,right}}$ in Fig. 6, are larger than those in the recovered sample designated $A_{\mathrm{Re,left}}$ and $A_{\mathrm{Re,right}}$. Considering the formation of these distorted materials, it follows that the effective contribution of grain boundary sliding to the total strain in the ultrafine-grained sample may be represented by the ratio

$$R(\%) = \frac{A_{\mathrm{HPT}} - A_{\mathrm{Re}}}{A_{\mathrm{HPT}}} \times 100 = \frac{\left(A_{\mathrm{HPT,left}} + A_{\mathrm{HPT,right}}\right) - \left(A_{\mathrm{Re,left}} + A_{\mathrm{Re,right}}\right)}{\left(A_{\mathrm{HPT,left}} + A_{\mathrm{HPT,right}}\right)} \times 100 \quad (1)$$

Measurements were taken along two mutually orthogonal directions at five selected Vickers patterns in both the recovered and the HPT-deformed samples thereby

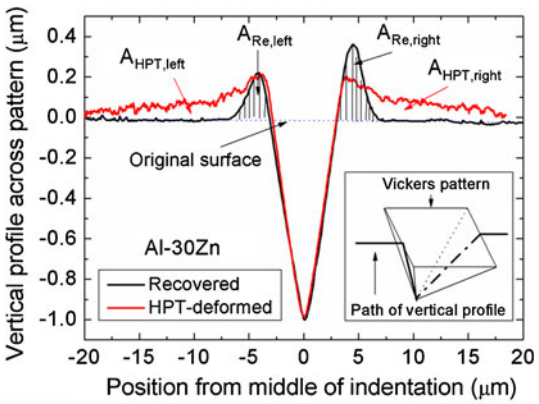

Fig. 6 Plot of the vertical profiles across the centers of the Vickers patters for samples in the recovered and HPT-deformed conditions: $A_{\mathrm{Re,left}}$ and $A_{\mathrm{Re,right}}$, plus $A_{\mathrm{HPT,left}}$ and $A_{\mathrm{HPT,right}}$, represent the areas of the pile-ups observed on the two opposite sides of the Vickers patterns for the recovered and HPT-deformed samples, respectively

giving a total of 10 separate measurements of A_{HPT} and A_{Re}. From these measurements, Eq. 1 was used to estimate the area values as $A_{\mathrm{HPT}} \approx 1.95$–$2.35\ \mu m^2$ and $A_{\mathrm{Re}} \approx 0.95$–$1.15\ \mu m^2$. Taking these estimates for A_{HPT} and A_{Re}, the value of R changes between 40 and 60%. These

calculations suggest, therefore, that grain boundary sliding makes a significant contribution to the accommodating strain in the ultrafine-grained sample especially when it is noted that measured sliding contributions of ~60% typically represent situations where all of the strain is produced by the sliding process [28].

The high value of the strain rate sensitivity and the estimated significant role of grain boundary sliding are mutually consistent and they both provide an explanation for the super-ductility observed in the Al–Zn alloy at ambient temperature. The reason for this unusual behavior can be attributed to the development of thin layers of a Zn-rich grain boundary phase, which leads readily to the occurrence of enhanced sliding. In this model, the high ductility state corresponds to the ultrafine-grained structure where large fractions of the Al/Al boundaries are wetted with thin Zn layers. This structure may be a consequence of a grain boundary wetting phase transformation in which the transformation proceeds at a temperature T_{wGB}, where the grain boundary energy, γ_{GB}, becomes higher than the energies $2\gamma_{SL}$ for the two solid/liquid interfaces or $2\gamma_{SS}$ for the two solid/solid interfaces [29–32].

From the bulk Al–Zn phase diagram, it is deduced that the Al–Zn system belongs to the classical system with a critical point for a binary solution [33]. In practice, boundary wetting by both the solid and liquid phases is feasible in the Al–Zn system due to the relatively low energy of the Al/Zn interfaces [34, 35]. Recent experiments measured the mean contact angle in polycrystalline Al–Zn between the Al/Al boundaries and boundary particles of the Zn phase after long anneals below the monotectoid temperature of $T_{mon} = 277$ °C [36]. These measurements show the contact angle decreases with decreasing temperature and a condition of full wetting by a Zn-layer is fulfilled at room temperature for all Al/Al boundaries. This means that all of the Al/Al boundaries are wetted by a layer of Zn at room temperature and this layer may be relatively thin depending on the Zn content and the time for equilibration. Moreover, during SPD processing and the formation of ultrafine grains, the vacancy concentration and the diffusion coefficient increase by ~4–5 times and the boundary energy increases by ~70–80% due to the appearance of an excess defect density [37, 38], which also contributes to the formation of this thin boundary layer of Zn. This hypothesis of forming lubricating Zn boundary layers in this alloy is supported by the estimation of the sliding contribution to the total ductility. Since the Zn wets the Al grain boundaries during grain refinement by SPD processing, it can be supposed that the Zn layer provides lubrication and thereby facilitates easier GB sliding and a consequent enhancement in ductility. The origin and role of the Zn layers will be checked experimentally in our on going studies.

Summary

This research suggests the potential for achieving high strength and high ductility in ultrafine-grained alloys using a GB wetting transition at room temperature. In principle, the high strength is ensured by the ultrafine grains of component A with a high melting temperature and the high ductility is ensured by the thin equilibrium wetting layers of component B having a lower melting temperature and lying along the A/A interfaces.

Acknowledgements We thank Mr. Peter Szommer for assistance with the AFM measurements. This work was supported by the Russian Foundation for Basic Research under Grants No. 08-08-97044 and 09-08-92656 and Federal Agency for Science and Innovations (RZV, MYuM, ARK), the Russian Foundation for Basic Research under Grants No. 09-03-92481, 09-03-00784 and 08-08-91302) (BBS), the Hungarian Scientific Research Fund, OTKA, under Grant No. K67692 and K81360 (NQC) and the National Science Foundation of the United States under Grant No. DMR-0855009 (TGL).

References

1. Valiev RZ, Islamgaliev RK, Alexandrov IV (2000) Prog Mater Sci 45:103
2. Valiev RZ, Estrin Y, Horita Z, Langdon TG, Zehetbauer MJ, Zhu YT (2006) JOM 58(4):33
3. Zhu YT, Liao X (2004) Nat Mater 3:351
4. Koch CC, Morris DG, Lu K, Inoue A (1999) MRS Bull 24:54
5. Wang Y, Chen M, Zhou F, Ma E (2002) Nature 419:912
6. Zhao YH, Bingert JF, Liao XZ, Cui BZ, Han K, Sergueeva A, Mukherjee AK, Valiev RZ, Langdon TG, Zhu YT (2006) Adv Mater 18:2949
7. Zhao YH, Zhu YT, Liao XZ, Horita Z, Langdon TG (2006) Appl Phys Lett 89:121906
8. Zhao YH, Liao XZ, Cheng S, Ma E, Zhu YT (2006) Adv Mater 18:2280
9. Horita Z, Ohashi K, Fujita T, Kaneko K, Langdon TG (2005) Adv Mater 17:1599
10. Tao KX, Choo H, Li HQ, Clausen B, Jin JE, Lee YK (2007) Appl Phys Lett 90:101911
11. Valiev R, Gunderov D, Prokofiev E, Pushin V, Zhu Y (2008) Mater Trans 49(1):97
12. Valiev R (2004) Nat Mater 3:511
13. Valiev RZ, Salimonenko DA, Tsenev NK, Berbon PB, Langdon TG (1997) Scripta Mater 37:1945
14. Langdon TG (2009) J Mater Sci 44:5998. doi:10.1007/s10853-009-3780-5
15. Murashkin MYu, Kilmametov AR, Valiev RZ (2008) Phys Met Metallogr 106(1):90
16. Zhilyaev AP, Langdon TG (2008) Prog Mater Sci 53:893
17. Klug HP, Alexander LE (1974) X-ray diffraction procedures for polycrystalline and amorphous materials. Wiley, New York
18. Chinh NQ, Gubicza J, Kovács Zs, Lendvai J (2004) J Mater Res 19:31
19. Straumal BB, Baretzky B, Mazilkin AA, Phillipp F, Kogtenkova OA, Volkov MN, Valiev RZ (2004) Acta Mater 52:4469
20. Mazilkin AA, Straumal BB, Rabkin E, Baretzky B, Enders S, Protasova SG, Kogtenkova OA, Valiev RZ (2006) Acta Mater 54:3933
21. Chinh NQ, Vörös Gy, Szommer P, Horita Z, Langdon TG (2006) Mater Sci Forum 503–504:1001

22. Meyer MA, Mishra A, Benson DJ (2006) JOM 58(4):41
23. Zhang K, Weertman JR, Eastman JA (2005) Appl Phys Lett 87:061921
24. Zhang K, Weertman JR, Eastman JA (2004) Appl Phys Lett 85:5197
25. Man J, Obrtlík K, Polák J (2003) Mater Sci Eng A 351:123
26. Man J, Petrenec M, Obrtlík K, Polák J (2004) Acta Mater 52:5551
27. Choi Y, Lee HS, Kwon D (2004) J Mater Res 19:3307
28. Langdon TG (1994) Mater Sci Eng A174:225
29. Straumal BB, Kogtenkova O, Zięba P (2008) Acta Mater 56:925
30. Straumal BB (2003) Grain boundary phase transitions. Nauka publishers, Moscow
31. Straumal BB, Mazilkin AA, Kogtenkova OA, Protasova SG, Baretzky B (2007) Philos Mag Lett 87:423
32. Straumal BB, Gornakova AS, Kogtenkova OA, Protasova SG, Sursaeva VG, Baretzky B (2008) Phys Rev B 78:054202
33. Massalski TB (ed) (1990) Binary alloy phase diagrams, 2nd edn. ASM International, Materials Park, OH, p 238
34. Straumal B, Valiev R, Kogtenkova O, Zieba P, Czeppe T, Bielanska E, Faryna M (2008) Acta Mater 56:6123
35. Gao YJ, Han YJ (2003) Mater Sci Forum 475–479:3131
36. Straumal BB, Kogtenkova OA, Protasova SG, Nekrasov AN, Baretzky B (2010) JETP Lett 92, in press
37. Kilmametov AR, Vaughan G, Yavari AR, LeMoulec A, Botta WJ, Valiev RZ (2009) Mater Sci Eng A 503:10
38. Valiev RZ, Kozlov EV, Ivanov YuF, Lian J, Nazarov AA, Baudelet B (1994) Acta Metall Mater 42:2467